Journal of Nuclear Materials 510 (2018) 603–612

Contents lists available at ScienceDirect

Journal of Nuclear Materials

journal homepage: www.elsevier.com/locate/jnucmat

Sintering behavior of UO_2–Er_2O_3 mixed fuel

Michelangelo Durazzo [a, *], Artur C. Freitas [a], Alberto E.S. Sansone [a], Nildemar A.M. Ferreira [a], Elita F. Urano de Carvalho [a], Humberto G. Riella [a, b], Ricardo M. Leal Neto [a]

[a] Nuclear and Energy Research Institute, IPEN/CNEN-SP, São Paulo, Brazil
[b] Chemical Engineering Department, Santa Catarina Federal University, Florianópolis, Brazil

HIGHLIGHTS

- Good sintered densities can be obtained up to 4 wt% Er_2O_3 in UO_2–Er_2O_3 mixed fuel.
- The sintering behavior of the UO_2–Er_2O_3 fuel is similar to the UO_2–Gd_2O_3.
- The homogeneity degree is mandatary in sintering UO_2–Er_2O_3 mixed fuel.
- A third phase was experimentally detected in the UO_2–Er_2O_3 system.

GRAPHICAL ABSTRACT

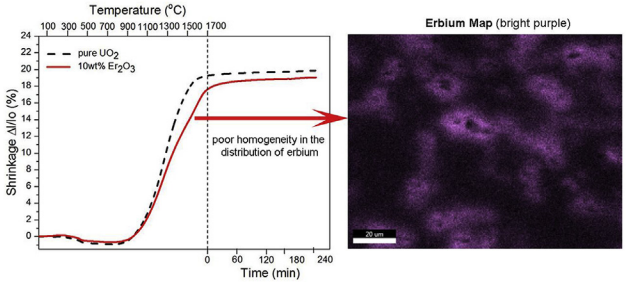

ARTICLE INFO

Article history:
Received 29 May 2018
Received in revised form
3 August 2018
Accepted 27 August 2018
Available online 29 August 2018

Keywords:
Nuclear fuel
Burnable poison
Erbium oxide
Uranium dioxide
Mixed fuel
Sintering

ABSTRACT

The incorporation of burnable neutron absorbers into nuclear fuel pellets is important regarding reactivity compensation, which enables longer fuel cycles. The dry mechanical blending route is the most attractive process to accomplish absorbers incorporation because of its simplicity. By using this route, the present work has investigated the sintering behavior of UO_2–Er_2O_3 mixed fuel. A comparison with UO_2–Gd_2O_3 sintering behavior was presented. The behavior of UO_2–Er_2O_3 fuel sintering was similar to that reported for UO_2–Gd_2O_3 fuel, e.g. two-stage sintering with two peaks in the shrinkage rate curves. The effect showed to be less pronounced for Er_2O_3. This was attributed to the characteristics of the Er_2O_3 powder particles used as raw-material, whose agglomerates can be more easily broken and thus better homogenized during the blending with UO_2 powder. These results confirmed that sinterability depends directly on the quality of the homogenization of the powders, as seen previously. A second phase was experimentally detected in the UO_2–Er_2O_3 system, but its impact on the sintering behavior of this mixed fuel has not yet been clarified.

1. Introduction

The need to improve reactor performance through longer cycle lengths and improved fuel use has become apparent since the beginning of commercial nuclear power generation. Among several modifications introduced therefore, the initial fuel enrichment has been increased. Hence, the reactivity gain of the fuel at the beginning of core life must be compensated by the introduction of additional neutron-absorber material, which also helps to shape

* Corresponding author. Av. Prof. Lineu Prestes, 2242, Cidade Universitária, CEP 05508-000, São Paulo, SP, Brazil.
E-mail addresses: mdurazzo@ipen.br (M. Durazzo), artur.freitas@ipen.br (A.C. Freitas), alberto.sansone@ipen.br (A.E.S. Sansone), namferre@ipen.br (N.A.M. Ferreira), elitaucf@ipen.br (E.F.U. de Carvalho), humberto.riella@ufsc.br (H.G. Riella), lealneto@ipen.br (R.M. Leal Neto).

https://doi.org/10.1016/j.jnucmat.2018.08.051
0022-3115/

the core power distributions. This is obtained through the use of a burnable neutron absorber homogeneously distributed within the fuel [1].

The distribution of the burnable absorber in the fuel pellets allows the control of the neutron population with the insertion of the control rods at a smaller distance. Besides, it is possible to place the fuel with burnable absorber in strategic positions, evenly distributing the reactivity and avoiding power peaks.

Furthermore, the traditional PWR (pressurized water reactor) fuel management scheme (without burnable absorber) is to load fresh fuel assemblies at the core periphery and move them toward the center of the core after the first cycle (out-in management). To minimize irradiation damage to the vessel, loading fresh fuel assemblies in outer positions must be avoided. An alternative fuel management scheme is now usually adopted consisting of fresh fuel assemblies loaded in the center of the core, which are then shifted to the core periphery for their last cycle (in-out management). This type of fuel management scheme is called "low leakage loading pattern" (LLLP) and requires that the power of the fresh fuel assemblies be depressed [2]. To accomplish that, burnable absorbers must be introduced in those fuel assemblies. This is an additional incentive for the use of burnable absorbers.

The progressive development of gadolinium as an integrated burnable absorber from 1 wt% - in the early utilizations in BWRs (boiling water reactors) - to the present level - 6 to 10 wt% in PWRs - has provided a large data base. This fact, along with the good performance of gadolinium fuel rods, has spread its utilization by most fuel suppliers [2].

However, by increasing gadolinium content, the thermal conductivity and melting point of the mixed fuel are affected to a significant extent, resulting in more complex nuclear design. These difficulties with high gadolinium content fuel have raised the search for alternative burnable absorbers, like ZrB_2 and erbium, both of which applied commercially [2].

The use of ZrB_2 as a burnable absorber was developed by Westinghouse under the designation IFBA (integral fuel burnable absorber). This IFBA fuel consists of a thin layer of ZrB_2 (0.02 mm) sputtered on the surface of the UO_2 pellets [3]. Among several advantages ZrB_2 IFBA provide a lower residual absorption penalty than the other discrete burnable absorber fuels, since it can be designed for complete depletion of the B-10 at the end of the first irradiation cycle.

Erbium has most of the advantages of the ZrB_2, such as a cross section similar to boron. The effective capture cross sections of erbium are well known and the double resonance peak at 0.5 eV plays a key role in managing the moderator temperature coefficient (MTC). This is the major advantage of erbium over ZrB_2. Typical difficulties of gadolinium, i.e. neutron spectrum hardening and wide neutron flux variations with gadolinium depletion are thereby avoided [4]. The potential interest of this burnable absorber compared to gadolinium is that the 167Er presents a relatively low absorption cross section in the thermal range and a non-negligible resonance integral that leads to a relatively slow consumption kinetic rather adapted to long or even very long cycles [4,5]. Erbium depletes relatively slower than gadolinium and boron. Therefore, erbium can be a rather effective burnable absorber for a reactor with a very long cycle [6]. Asou and Porta [7] suggest that gadolinium is more suitable for application as an integrated burnable absorber for cycles up to 18 months, while erbium, also as an integrated burnable absorber, is indicated for use in cycles of 24 months or longer.

Erbium is present in lower concentrations than gadolinium and distributed in a larger number of fuel rods. Gd_2O_3 is used commercially in a proportion up to 10 wt% homogeneously mixed with UO_2 and distributed in 3–6% of the fuel rods. Er_2O_3 is mixed with UO_2 in a proportion of 1–2.5 wt% and distributed in 20–30% of the fuel rods [2]. However, there are studies for integrated UO_2–Er_2O_3 fuels using concentrations up to 12 wt% Er_2O_3 enriched with the 167Er isotope.

Ranier and Grossbeck [8] studied the neutron performance of several burnable poisons, such as ZrB_2, gadolinium, samarium, erbium, dysprosium, europium and hafnium. In their work, additions of Er_2O_3 in the proportions from 2 to 12 wt% to the UO_2 powder (enrichment of 4.5 wt% 235U) were studied. The results indicate that there is a clear advantage in the use of erbium enriched in 167Er isotope regarding the initial reactivity and the end-of-cycle penalty as well.

Franceschini and Petrović [9] evaluated the performance of erbium as a burnable poison added to UO_2 fuel with 235U enrichment of 4.95 wt%. Er_2O_3 concentrations varied from 0.40 to 1.95 wt %. Four erbium isotopic compositions were studied. The authors concluded that when all 166Er is removed, the gain in cycle length is as high as 6.7%, justifying the economic viability of the isotopic modification of natural erbium.

Barchevtsev et al. [10] proposed a new concept of erbium doped uranium oxide fuel cycle for Light Water Reactors. The authors identified advantages in using a sequence of two irradiation cycles in different reactor types, i.e., a pressure water reactor (PWR) and a pressure tube graphite reactor (PTGR). The synergism can extend the fuel burnup from 100GWd/tHM in the PWR to 140GWd/tHM of the PTGR. The initial fuel uses 9.8 mol% isotopically modified erbium (5.8% of 166Er and 4.0% of 167Er) added to 19.8% enriched UO_2 fuel.

Concerning the fabrication of burnable absorber doped fuels, a number of studies related to the effects of a burnable poison addition, such as Gd_2O_3, on UO_2 sintering behavior have been published [11–15]. The UO_2–Gd_2O_3 fuel shows a quite different behavior on sintering when compared to the traditional pure UO_2 fuel. The incorporation of Gd_2O_3 has a harmful effect on UO_2 sintering behavior. Above 1200 °C, sintering rate decreases, and the final sintered density is significantly lower. Even small additions of Gd_2O_3 (2 wt%) causes this undesirable behavior.

Since there are few reports on the sintering behavior of Er_2O_3 doped UO_2 pellets, the purpose of this work is to study it. Published neutronic analyzes [8,10] have shown that the Er_2O_3 content to be incorporated into the standard UO_2 fuel can reach values above 2.5 wt%, which has been used commercially [2]. Therefore, in this work Er_2O_3 concentrations ranged from 1 to 10 wt%. The erbium distribution in the pellet after sintering is evaluated, as well as the possible formation of other phases than fluorite. Discussion is carried out by comparing the present results with those obtained for UO_2–Gd_2O_3 fuel.

2. Experimental

All the UO_2–Er_2O_3 samples used in this work were dry blended as previously described for UO_2–Gd_2O_3 [11,16,17]. UO_2 and Er_2O_3 powders were blended in a Turbula T2C shaker mixer for 1 h. Interlaced wires were used inside the homogenization vessel to promote breaking of agglomerates. The sample size for each composition was 20 g, being the powders homogenized in a single step. Er_2O_3 contents chosen in this work were 1, 2.5, 4 and 10 (wt%). Aluminum distearate (ADS) was added to the mixtures as a solid lubricant (0.2 wt% - constant).

UO_2 and ADS powders were supplied by INB (Indústrias Nucleares do Brasil) [18] and are routinely used in the current manufacturing of UO_2 pellets. The UO_2 powder was obtained from uranium hexafluoride via AUC (ammonium uranyl carbonate) conversion [16,19]. The Er_2O_3 powder was supplied by Alfa-Aesar (reference 11309) with purity 99.99%. Tables 1 and 2 present

Table 1
- Main physicochemical data for the UO_2 powder.

	actual	Specification[a]
O/U	2.0818	2.08–2.30
U_{total} (%)	87.574	≥86.8
enrichment 235U (%)	4.137	4.10–4.15
moisture (wt%)	0.15	≤0.4
surface area (m^2/g)	5.0	2.5–6.0
bulk density (g/cm^3)	2.2	2.0–2.6
flowability (s/50 g)	4.6	≤10
mean particle size (μm)	30.04	<200[b]
Impurities (μg/gU)		
F	5.312	≤100
Al	1.777	≤250
Ca	4.212	≤25
B	<0.2	≤0.5
Fe	15.24	≤100
Ni	0.421	≤50
Si	6.916	≤100
Gd	0.2	≤1

[a] Specification for the UO_2 powder manufactured by INB for the Brazilian PWR-type ANGRA-1 and ANGRA-2 reactors.
[b] Maximum of 2 wt% between 100 μm and 200 μm.

physicochemical data for UO_2 and Er_2O_3 powders, respectively. Scanning electron microscopy (SEM) images of UO_2 and Er_2O_3 powders were obtained with a Jeol JSM 60102A with secondary electrons and are shown in Fig. 1. UO_2 particles shape (Fig. 1a) is typical for AUC-derived powders, as expected. Fig. 2 presents the particle size distribution of both powders, which were determined by a CILAS laser diffraction particle size analyzer model 1064, operating with 820 nm laser and using water as liquid medium and sodium tetra pyrophosphate as dispersing agent.

Mixed oxide powders with 0.2 wt% of ADS were compacted in cylindrical steel die (10 mm internal diameter) with pressures ranging from 295 to 353 MPa. For apparent density calculation green pellets were individually weighed in a semi-analytical balance (0.0001 g) and its volume was determined assuming cylindrical shape. Height and diameter of the pellets were measured with a 0.01 mm precision caliper. Theoretical density (TD) of the mixtures were calculated considering component densities of 10.96 g/cm^3 (for UO_2) [20], 8.65 g/cm^3 (for Er_2O_3) [21] and 1.009 g/cm^3 (for ADS) [22,23]. Apparent densities of the green pellets ranged from 51 to 52% of TD with mean diameter and height of 10.3 mm and 11.2 mm, respectively (Table 3).

Samples were sintered in a Setaram Setsys 1700 dilatometer at 1700 °C for 240 min under pure hydrogen atmosphere. The heating rate was 5 °C/min, the same used previously with UO_2–Gd_2O_3 [15], to allow a comparison with the sintering behavior of UO_2–Er_2O_3. Sintered densities were determined by measuring the weight of the samples immersed in water according to the Archimedes' principle [24].

Table 2
Some physicochemical data for Er_2O_3 powder.

Impurities	(μg/g)
Dy_2O_3	5
Ho_2O_3	5
Tm_2O_3	44
Yb_2O_3	5
Y_2O_3	5
Fe_2O_3	5
Si_2O_3	20
CaO	40
loss on ignition (wt%)	0.10
moisture (wt%)	0.25
mean particle size (μm)	11.04

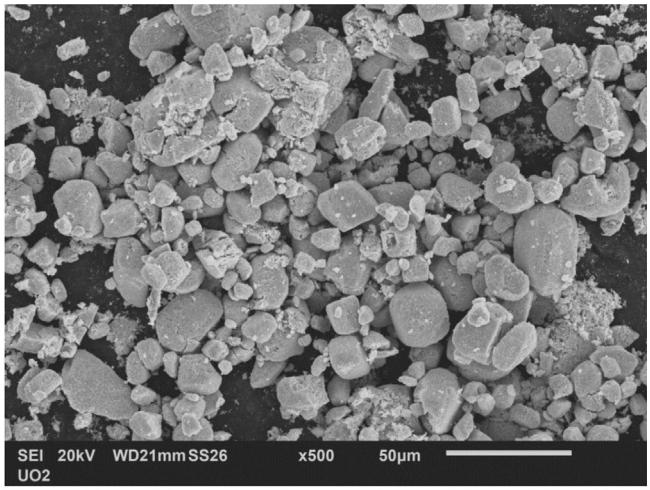

(a)

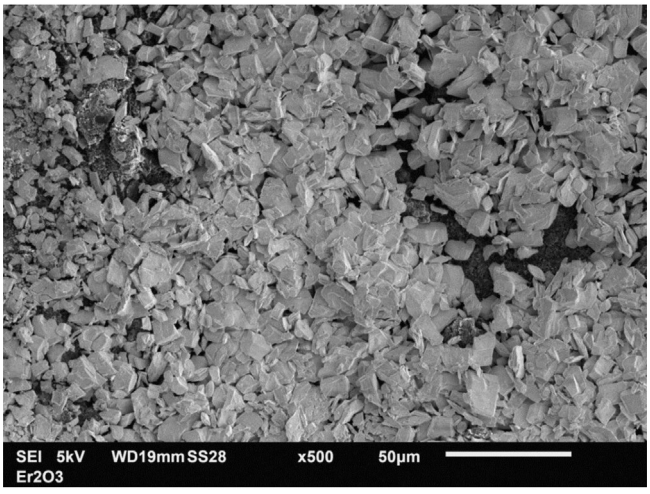

(b)

Fig. 1. SEM images (secondary electrons) showing particles size and morphology: (a) UO_2; (b) Er_2O_3.

After sintering, microstructural characterization was accomplished by scanning electron microscopy (SEM) and X-ray diffraction (XRD) analyzes on polished sections of the pellets. Samples were sanded sequentially in 400–1200 grid sandpapers and polished with 3 μm and 1 μm diamond. A SEM-FEG (Jeol - JSM-6701F) was used with secondary and backscattered electrons. EDS mapping of erbium and uranium was performed with 120 min of counting time at 15 KV. DRX analyses were performed on powdered sintered pellets using Cu-Kα radiation in a Bruker's D8 Advance diffractometer. Diffraction patterns were obtained at room temperature with both, anti-scattering and divergent slits of 1.0 mm and a 0.4 mm receiving slit. The measuring step was 0.02°, with counting time at each step of 10 s.

3. Results and discussion

Fig. 3a shows the linear shrinkage curves from the sintering of UO_2–Er_2O_3 pellets. The first region of the curves (300–450 °C) shows an expansion that can be explained by UO_2 formation from the reduction of U_4O_9, initially present in the UO_2 powder (O/U = 2.08). Like Gd_2O_3, the presence of Er_2O_3 causes significant changes in the traditional sintering behavior of typical pure UO_2

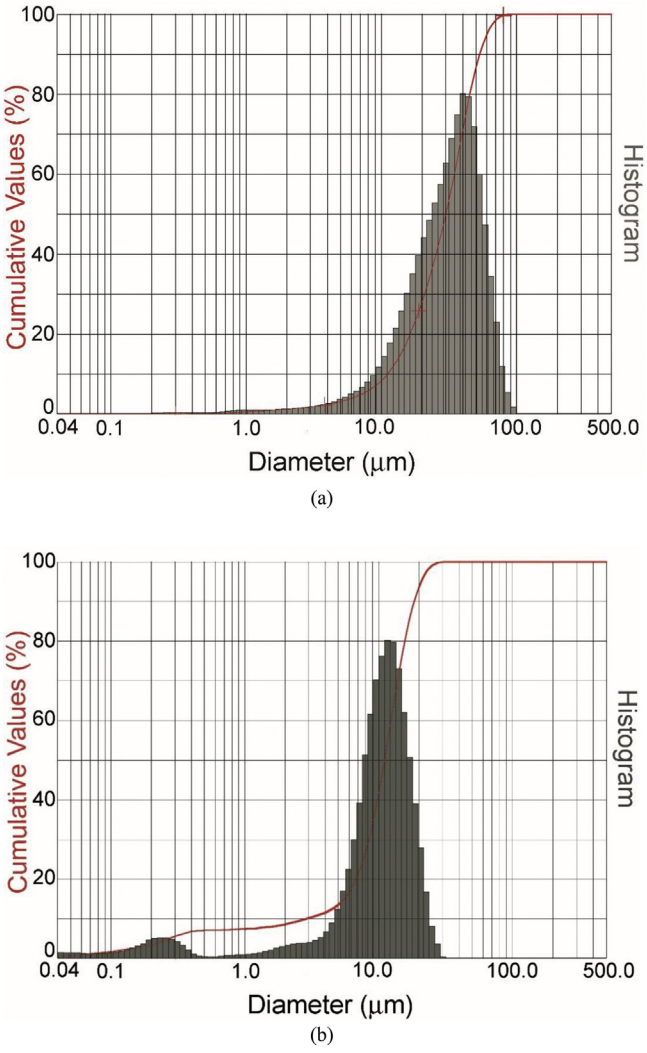

Fig. 2. Particle size distribution of (a) UO_2 and (b) Er_2O_3 powders.

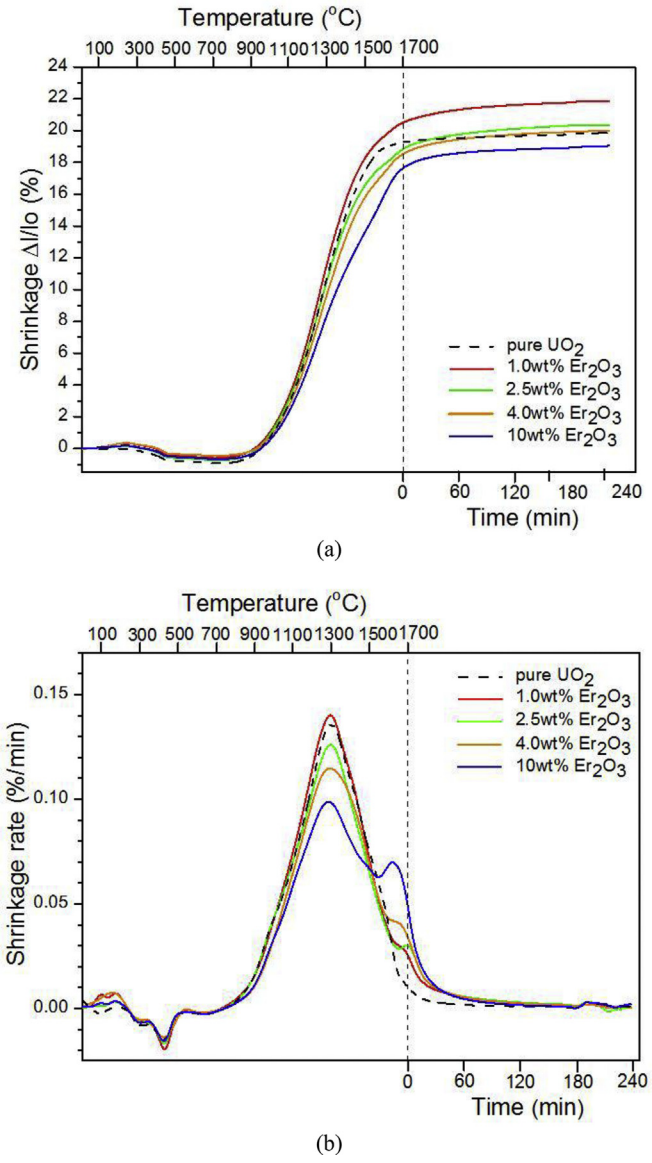

Fig. 3. Effect of Er_2O_3 content on the sintering behavior of UO_2–Er_2O_3 fuel pellets (heating rate = 5 °C/min): (a) Linear shrinkage; (b) Shrinkage rate.

fuel, but the effect is quite different. For small addition, such as 1 wt %, Er_2O_3 improves sintering, resulting in 2% higher shrinkage than for pure UO_2. Moderate additions of Er_2O_3 (between 2.5 and 4 wt%) cause total shrinkage comparable to the sintering of pure UO_2. Higher addition of Er_2O_3, such as 10 wt%, causes a decrease in shrinkage of about 1%. As for shrinkage rate during sintering (Fig. 3b) the maximum value occurred at 1290 °C whatever the Er_2O_3 content. Shrinkage rates however was lower the greater the Er_2O_3 content. The shrinkage rate recovers from 1535 °C and reaches a new maximum at 1620 °C for 10 wt% Er_2O_3. The recovery is greater the higher the Er_2O_3 content. The lower the Er_2O_3 content, the higher is the temperature for the recovery of the shrinkage rate.

Table 3
Green pellet apparent densities.

Er_2O_3 content (wt%)	Green density (g/cm^3)	$TD_{mixture}$ (g/cm^3)	Green density (%TD)
pure UO_2	5.55	10.75	51.64
1.0	5.50	10.72	51.31
2.5	5.47	10.68	51.23
4.0	5.50	10.64	51.71
10	5.39	10.48	51.44

(TD = Theoretical Density).

This two-stage sintering behavior, here denoted by two peaks in the shrinkage rate curves, is also typically observed in the UO_2–Gd_2O_3 system [11–15]. Dilatometric analyses of UO_2–Gd_2O_3 samples showed that around 1200 °C the shrinkage was delayed, the sintering rate was decreased and densification was shifted to higher temperatures. The shrinkage rate recovered from 1350 °C and reached a new maximum at temperatures that depend on the Gd_2O_3 content (about 1500 °C for 2 wt% Gd_2O_3). This phenomenon, denominated "sintering blockage", was discussed in previous works [14,15] and was seen when Gd_2O_3 powder was added to AUC-derived UO_2 powder by the dry mechanical blending route.

The mechanism proposed to explain the abnormal sintering behavior of UO_2–Gd_2O_3 fuel is based on pore formation due to the Kirkendall effect [15]. Other authors have proposed a mechanism based on the formation of low diffusivity Gd-rich $(U,Gd)O_2$ phases that could actuate as a diffusion barrier during the sintering process [11,25,26]. Manzel and Dörr [11] attributed the low densities of sintered UO_2–Gd_2O_3 pellets to the formation of a solid solution together with densification. Since these two processes resulted

from interdiffusion, there is a decrease in the sintering rate which shifts densification to higher temperatures. Assmann et al. [25] complemented this subject by proposing that the diffusion coefficients in the UO_2–Gd_2O_3 system show a complex dependence on the U:Gd:O ratio of the oxide phases formed. Peehs et al. [26] detected the presence of the $(U_{0.5}Gd_{0.5})O_2$ phase in sintered UO_2–Gd_2O_3 pellets; however, their report did not discuss the possible participation of that phase on the sintering mechanism.

The sintering curves shown in Fig. 3a are similar in shape to the curves obtained for the UO_2–Gd_2O_3 system [11–15], indicating that the same sintering blockage mechanism is acting for both systems. However, in the case of UO_2–Er_2O_3 the phenomenon is much less pronounced. The decrease in linear shrinkage is smaller and occurs at much higher temperatures than those observed for the UO_2–Gd_2O_3 system. For concentrations up to 4 wt% Er_2O_3, the sintering blockage is difficult to visualize in the curves of Fig. 3a, but are perceptible in the curves of Fig. 3b, which shows the shrinkage rates. For the concentration of 10 wt% Er_2O_3, the phenomenon is more clearly observed.

The density variation of the sintered pellets with the content of Er_2O_3 and Gd_2O_3 [17] is compared in Fig. 4. In both cases, the mixed powders were prepared by the dry blending technique. The specified limits for the density of UO_2–Gd_2O_3 sintered pellets are indicated in the figure, which should be in the range of 93.5–96 % TD [27]. These limits were assumed to be valid for the UO_2–Er_2O_3 fuel.

The value for the TD of mixed oxides is a controversial issue. For the UO_2–Gd_2O_3 fuel some publications take the values calculated from the lattice parameter of the fluorite structure, assuming the formation of a perfect solid solution [28–30]. Since the samples used were prepared by the co-precipitation method, this assumption is valid and was confirmed experimentally in previous works [17,31]. On the other hand, some UO_2–Gd_2O_3 fuel specifications assume that no solid solution is formed in the calculation of the theoretical density [2,27]. In fact, experience shows that when the dry mechanical mixing route is adopted in the UO_2–Gd_2O_3 pellet manufacture what occurs is a combination of these two extremes. Gd_2O_3 dissolves in the fluorite lattice of UO_2 (starting from 1200 °C) but the gadolinium is not perfectly homogenized in the UO_2 matrix during sintering, remaining a concentration gradient around the original Gd_2O_3 sites [15].

In the case of the UO_2–Er_2O_3 fuel most of the Er_2O_3 dissolves in the fluorite structure of UO_2, as will be discussed in due course. Thus, TDs for the UO_2–Er_2O_3 system, which were used for plotting the data shown in Fig. 4, were calculated using the following expression, developed by Fedotov et al. [30] for the $(U,Er)O_2$ solid solution:

$$TD_{(U,Er)O2} = 10.9616 - 0.0175\ wt\%Er_2O_3 \quad (1)$$

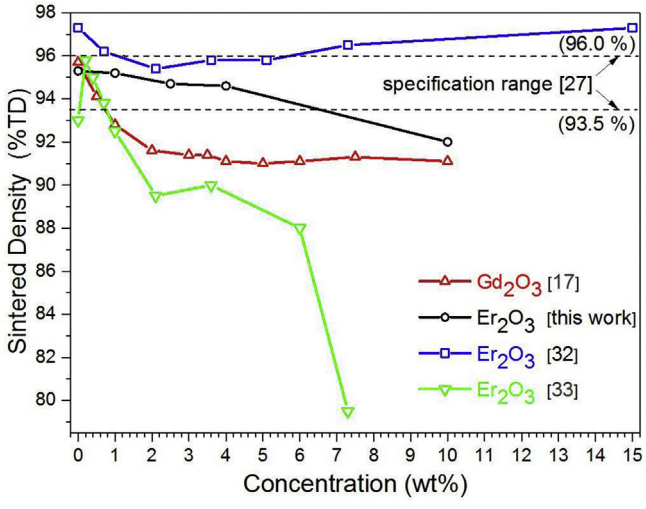

Fig. 4. Effect of Er_2O_3 content on the density of UO_2–Er_2O_3 pellets after sintering at 1700 °C for 4 h. The effect of Gd_2O_3 is also shown for comparison (1650 °C, 3 h).

Fig. 4 shows that Er_2O_3 impairs the sintering of UO_2. The higher the Er_2O_3 concentration, the lower the final density reached by UO_2–Er_2O_3 sintered pellet. Although the experimental conditions were not exactly the same (different UO_2 powders, green densities and sintering conditions), which makes comparison difficult, the effect of Er_2O_3 is not as pronounced as in the case of the UO_2–Gd_2O_3 fuel, which exhibits a density sharp drop at usual low Gd_2O_3 contents [17]. For UO_2–Er_2O_3 the decrease in the sintered density is smoother and almost linear. Based on the specification requirements of the UO_2–Gd_2O_3 fuel (93.5–96 %TD [27]), 4 wt% Er_2O_3 or less could be properly incorporated.

Results published for samples prepared in order to obtain perfect $(U,Er)O_2$ solid solutions [32,33] were also plotted in Fig. 4. Kim et al. [32] used co-milling for 6 h to prepare the samples for measuring lattice parameters. High sintered densities were observed at concentrations up to 15 wt% Er_2O_3. Similarly to the case of Gd_2O_3 [17,31], the incorporation of the erbium through the co-milling of UO_2 and Er_2O_3 powders promotes the sintering of the system, according to the mechanism proposed by Ho and Radford [34] for the UO_2–Gd_2O_3 system. Possibly the same mechanism may be acting, where U^{+5} ions are formed when Er^{+3} ions substitute the U^{+4} ions originally present in the UO_2 lattice structure. The smaller size of the U^{+5} ion formed causes the diffusivity to be greatly enhanced and the sintered density is higher. This would explain the higher densities obtained by Kim et al. [32]. The results obtained by Yamanaka et al. [33] showed divergent results probably due to the method for sample preparation, which used multiple heat treatments. This makes it difficult to compare the results and the understanding of the cause for the divergent results.

Fig. 5 shows a comparison between the sintering behavior of the UO_2–Er_2O_3 fuel and UO_2–Gd_2O_3 fuel (data from reference [15]). The technique for the preparation of the mixed powders was the same (dry blending), which allows the comparison, although with some caution due to the differences in the experimental conditions. For the comparison, the shrinkage rates obtained from Ref. [15] were normalized based on the maximum shrinkage rate of the pure UO_2 pellet of the present work. A decrease of 26% in the maximum shrinkage rate in the first peak was observed for the concentration of 2 wt% Gd_2O_3, while a decrease of only 7% was seen in the case of 2.5 wt% Er_2O_3. For 5 wt% Gd_2O_3, the decrease was 32%, against 15% for 4 wt% Er_2O_3. For 10 wt% Gd_2O_3, the decrease was 48%, against 26% for 10 wt% Er_2O_3. These results show that the densification recovery after the sintering blockage is more difficult for the UO_2–Gd_2O_3 system than for the UO_2–Er_2O_3 system. Therefore, the sintering blockage is much more severe for UO_2–Gd_2O_3 than for UO_2–Er_2O_3, thus leading to a larger decrease in the shrinkage rate at the first peak, which turns the densification recovery more difficult in subsequent sintering. This could explain the higher sintered densities of the UO_2–Er_2O_3 pellets compared to those of UO_2–Gd_2O_3, as shown in Fig. 4.

Fig. 6a and d shows SEM images (secondary electrons) of the pore structure of the sintered pellets. Er_2O_3 added to UO_2 causes the formation of "islands" of small clustered pores around large ones. These islands are not present in the sintered pellets of pure UO_2 and became larger and more frequent the higher the Er_2O_3 content.

Secondary and backscattered electron images from sample with

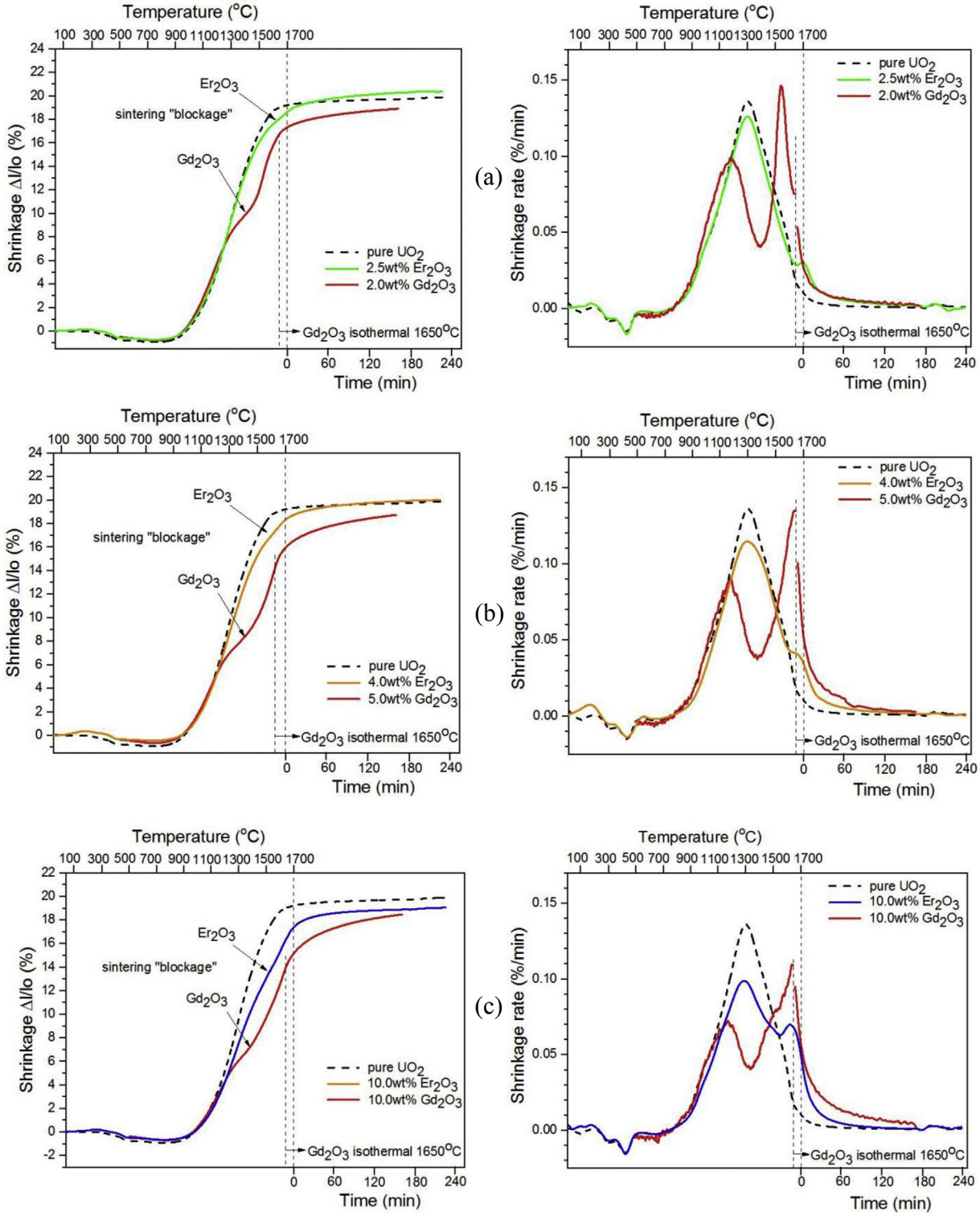

Fig. 5. Comparison between the sintering behavior of the UO_2–Er_2O_3 and UO_2–Gd_2O_3 fuels. (a) Er_2O_3/2.5 wt%,Gd_2O_3/2 wt%, (b) Er_2O_3/4 wt%,Gd_2O_3/5 wt%, (c) Er_2O_3/10 wt%,Gd_2O_3/10 wt%.

10 wt% Er_2O_3 were compared in Fig. 6e and f, respectively. A darker shade of gray area (Fig. 6f) can be observed surrounding the clustered pores, which indicates the presence of a lighter element than uranium in these regions. These darker regions are also observed in samples from the other compositions but are more clearly seen as the Er_2O_3 content is increased. Besides, the pore shape is similar to the shape of the original Er_2O_3 particles shown in Fig. 1b, with sharp corners and angled edges. This is best visualized in the image obtained with secondary electrons, shown in Fig. 6e.

Fig. 7 shows EDS mapping for erbium and uranium. A direct qualitative comparison between all the erbium mappings is possible, since they were performed under the same conditions. It

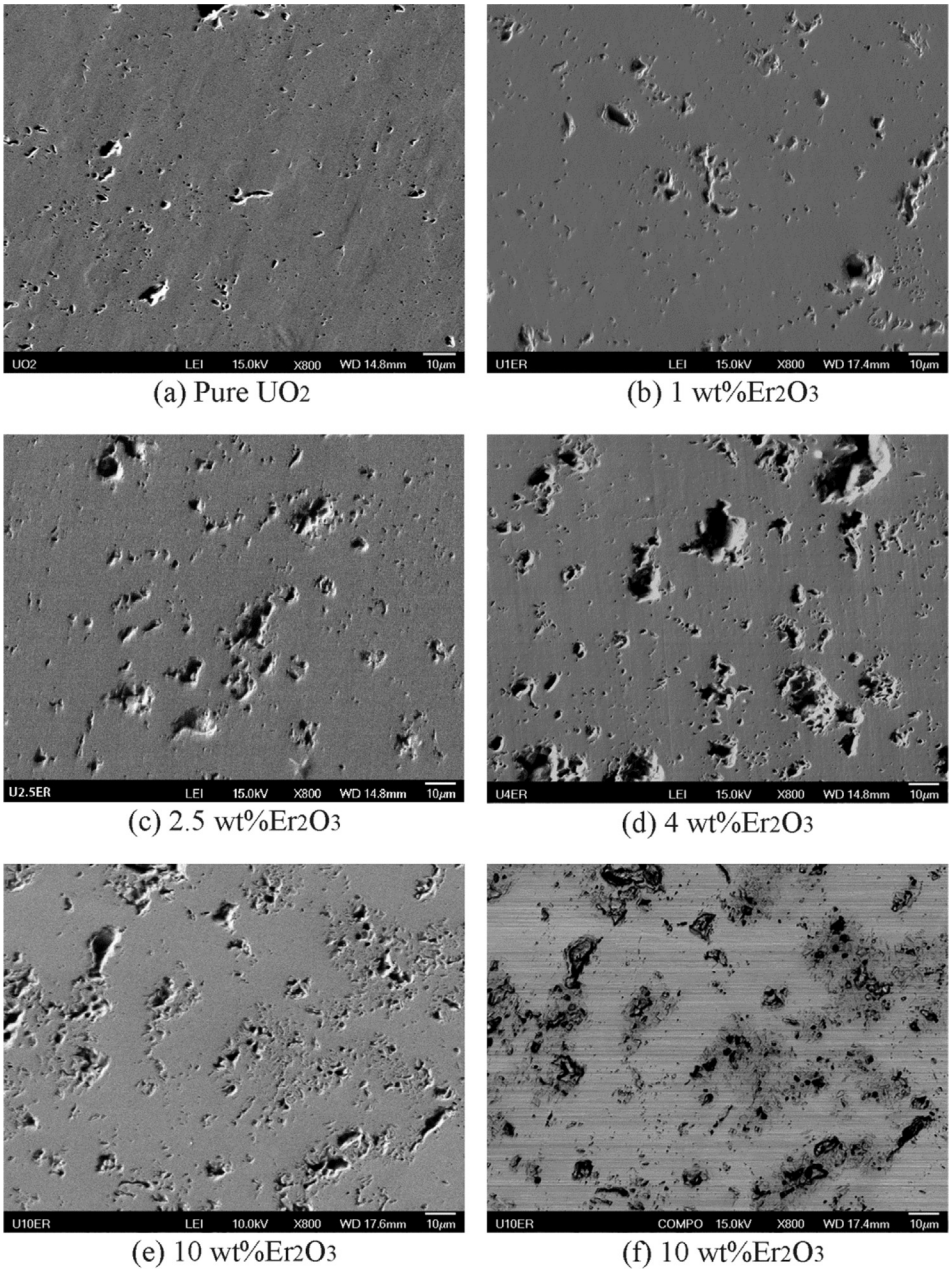

Fig. 6. Secondary (a to e) and backscattered (f) electrons images from the microstructure of the sintered UO_2–Er_2O_3 pellets (Er_2O_3 contents are indicated).

can be noticed that there is a higher concentration of erbium surrounding the clustered pores (compared to the matrix), denoted by the light areas in erbium mapping, corresponding to the darker areas in the backscattered electron image shown in Fig. 6f. These concentrated erbium regions increases in extension with the increase of the Er_2O_3 content and are always associated with the clustered pore regions. An erbium concentration gradient is formed when the erbium particles solubilize in the UO_2 structure as well. A "cloud" forms around the clusters of pores which decreases in intensity as the distance from the center of the pore region increases, indicating the decrease of the erbium concentration.

These results suggest that the clusters of pores are formed by original agglomerates of Er_2O_3 particles that were not completely broken during the powders blending step. These particle agglomerates are absorbed by the UO_2 matrix giving rise to observed clustered pores. The primary Er_2O_3 particles diffuse into the UO_2 matrix leaving behind the pores as a result of the Kirkendall effect. This behavior is similar to that found in the UO_2–Gd_2O_3 fuel [15]. However, images from Fig. 1b suggests that Er_2O_3 agglomerates are less cohesive than Gd_2O_3 agglomerates (see Fig. 2 on [15]) and are more easily broken during the blending step, thus splitting into small agglomerates or even into individual particles. This mechanical deagglomeration is more efficient as the Er_2O_3 content is lower, as revealed by the images form Figs. 6 and 7 In the Er_2O_3 case, the pores formed are smaller and more spaced, which could explain the better sinterability of the UO_2–Er_2O_3 pellets when compared to those of UO_2–Gd_2O_3.

Although gadolinium-rich phases have been indirectly detected in previous work [14], experimental results have shown that their presence is not responsible for the sintering blockage in the UO_2–Gd_2O_3 fuel [35]. However, the formation of phases different of the fluorite in the UO_2–Er_2O_3 fuel could explain the high

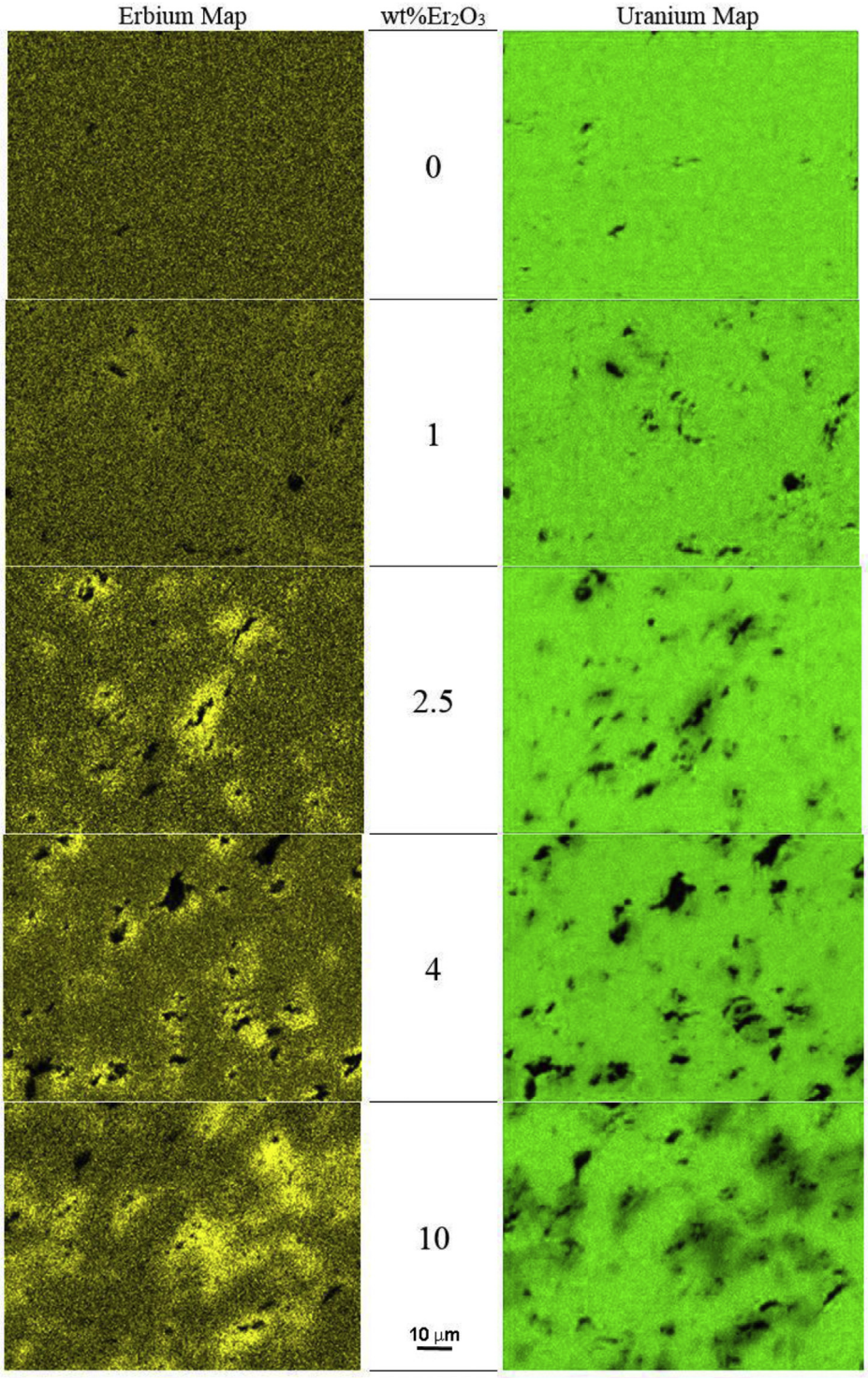

Fig. 7. EDS Mapping from Er and U elements (Er_2O_3 content is indicated).

temperature at which the erbium solubilization occurs in the UO_2 fluorite lattice (above 1500 °C), substantially higher than the temperature associated with gadolinium solubilization (around 1350 °C).

Fig. 8 shows X-ray diffraction patterns obtained from UO_2–Er_2O_3 sintered pellets grounded to powder. No Er_2O_3 peaks were observed in the diffraction patterns, which indicate that erbium was dissolved in the UO_2 fluorite structure. However, instead of forming a single phase solid solution, second phase peaks can be observed. This second phase has the same set of reflections as the first one, but shifted to the right (as seen clearer with 10 wt% Er_2O_3), i.e. it has also a fluorite-type structure, but with a smaller lattice parameter. The presence of a second phase is more evident for pellets with higher amounts of Er_2O_3, since the intensities of the emerging phase's reflections increase along with the Er_2O_3 content in the pellet, which means the second phase's fraction increases as

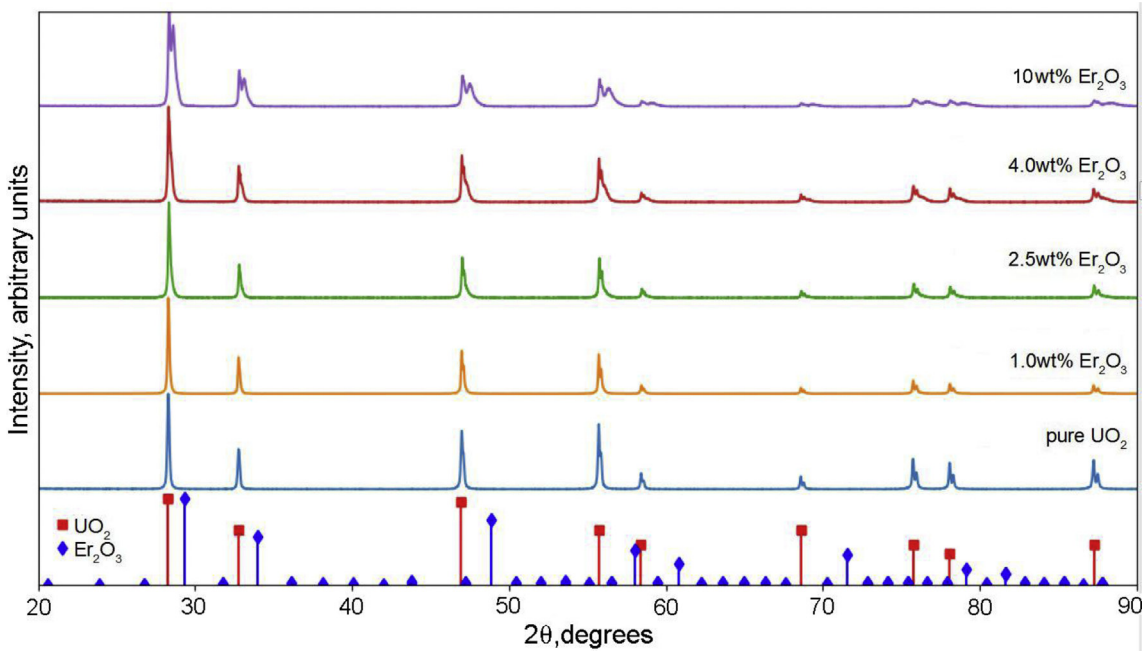

Fig. 8. Diffraction patterns of the pellets analyzed. At the bottom, the reflections for the structures of the UO_2 and Er_2O_3 powders used to make the pellets.

a function of Er_2O_3 content.

The peaks of this second phase can be resolved visually for the pellets with 4.0 and 10 wt% Er_2O_3. For the 1.0 and 2.5 wt% Er_2O_3 pellets, even though the second phase's maxima do not appear separated from the maxima of the first phase, they still can be seen as "tails" to the right of each peak. For the pellet with 1.0 wt% Er_2O_3, these tails are less evident, but their effects on the peak profiles can be perceived, especially at higher angles, when comparing the diffraction patterns for the doped and undoped pellets.

This effect of Er_2O_3 on the diffraction pattern was not observed by Yamanaka et al. [33] and Kim et al. [32] probably because these authors prepared samples to obtain solid solutions, so erbium was perfectly dissolved in the UO_2 fluorite structure. In the present work, the case is different, since the samples do not show homogeneity at the atomic level, having a gradient of erbium concentration around the original particles of Er_2O_3, as shown in Figs. 6f and 7.

The formation of a second phase around the originally present Er_2O_3 particles may possibly hinder the diffusion of erbium into the fluorite lattice of UO_2, which may have displaced the solubilization of the erbium to higher temperatures when compared to the temperature at which the solubilization occurs in the case of gadolinium. Further work needs to be performed to study the presence of this phase in the UO_2–Er_2O_3 system and its role in the sintering blockage mechanism observed for this mixed fuel.

The results from the present work confirm the observations and conclusions of previous works for the UO_2–Gd_2O_3 system. The impact of the homogeneity of Gd_2O_3 distribution greatly influences the sintering of the system and the final reached density [17,31]. Very high densities (~99% TD) can be achieved after sintering if the homogeneity degree of the gadolinium distribution in the mixed fuel is at the atomic level (or even at the microscope level). In this case the sintering curves do not show the two shrinkage steps that characterize the sintering blockage [17]. These same conclusions seem to be valid for the UO_2–Er_2O_3 system.

Manufacturing the UO_2–Er_2O_3 fuel by the co-precipitation or co-milling routes would likely result in sintered pellets with high densities that could easily meet any specifications. However, these routes are not industrially attractive because they deeply modify the manufacturing technology of the traditional UO_2 fuel. The co-milling route has the important disadvantage of destroying the morphological characteristic of the UO_2 powder derived from the AUC, whose high flowability is important for compaction step.

Therefore, the results indicate that the sintering blockage problem can be solved after the development of an improved procedure to ensure a high degree of homogenization in the dry mechanical blending of the powders. This is valid for both integrated burnable poison fuels, UO_2–Er_2O_3 and UO_2–Gd_2O_3. Development of this procedure is in progress.

4. Conclusions

The sintering behavior of UO_2–Er_2O_3 fuel was similar to that reported for UO_2–Gd_2O_3 fuel, occurring in two stages with two peaks in the shrinkage rate curves. However, the effect is less pronounced for Er_2O_3.

For small contents, such as 1 wt%, the presence of Er_2O_3 improves sintering, resulting in high shrinkage, up to 2% higher than for pure UO_2. Moderate Er_2O_3 additions (between 2.5 and 4 wt%) cause total shrinkage comparable to the sintering of pure UO_2. High Er_2O_3 additions, such as 10 wt%, cause a decrease in shrinkage of about 1%. Based on the specification requirement for the UO_2–Gd_2O_3 fuel (93.5–96 %TD), sintering with Er_2O_3 contents up to 4 wt% can be accomplished concerning the dry mechanical method for UO_2 ex-AUC and Er_2O_3 powders dry mechanical blending.

The better sinterability of the UO_2–Er_2O_3 fuel when compared to the UO_2–Gd_2O_3 fuel is attributed to the own characteristics of the Er_2O_3 powder particles used here, which forms agglomerates that are more easily broken during blending with the UO_2 powder. These results confirm that sinterability depends directly on the quality of the homogenization of the powders as seen previously. Therefore, it is mandatory to develop an improved procedure for dry mechanical blending of the powders with a high degree of homogeneity.

A second phase was experimentally detected in the UO_2–Er_2O_3

system, but its impact on the sintering behavior of this mixed fuel has not yet been clarified. Further work on this subject is in progress.

Acknowledgments

The authors are grateful for financial support to this work provided from CAPES-Eletronuclear.

Appendix A. Supplementary data

Supplementary data related to this article can be found at https://doi.org/10.1016/j.jnucmat.2018.08.051.

References

[1] W.K. Anderson, J.S. Theilacker, Neutron Absorber Materials for Reactor Control, USAEC, Naval Reactors, Division of Reactor Development, Washington, D.C., 1962.
[2] International Atomic Energy Agency, Characteristics and Use of Urania-gadolinia Fuels, Vienna, Austria, 1995. IAEA-TECDOC-844.
[3] R.L. Simmons, N.D. Jones, F.D. Popa, D.E. Mueller, J.E. Pritchett, Integral fuel burnable absorbers with ZrB_2 in PWRs, Nucl. Tech. 80 (3) (1988) 343–348. https://doi.org/10.13182/NT88-A34058.
[4] A. Jonsson, Initial physics evaluation of erbium as a burnable absorber in a PWR, Trans. Am. Nucl. Soc. 61 (1990) 340–341.
[5] J. Porta, M. Asou, Alternative poison? Stabilization additive? What future? Prog. Nucl. Energy 38 (2001) 347–350. https://doi.org/10.1016/S0149-1970(00)00132-3.
[6] A. Abdelghafar Galahom, Investigation of different burnable absorbers effects on the neutronic characteristics of PWR assembly, Ann. Nucl. Energy 94 (2016) 22–31. https://doi.org/10.1016/j.anucene.2016.02.025.
[7] M. Asou, J. Porta, Prospects for poisoning reactor cores of the future, Nucl. Eng. Des. 168 (1997) 261–270. https://doi.org/10.1016/S0029-5493(96)01322-2.
[8] J.P.A. Renier, M.L. Grossbeck, Development of Improved Burnable Poisons for Commercial Nuclear Power Reactor, OAK Ridge National Laboratory. Oak Ridge, Tenn., 2001. ORNL/TM-2001/238.
[9] F. Franceschini, B. Petrovic, Use of isotopically modified erbium to improve fuel cycle economics in IRIS, in: 5th International Conference on Nuclear Options in Countries with Small and Medium Electricity Grids, Croatia, 2004.
[10] V. Barchevtsev, V. Artisyuk, H. Ninokata, Concept of erbium doped uranium oxide fuel cycle in light water reactors, J. Nucl. Sci. Technol. 39 (2002) 506–513. https://doi.org/10.1080/18811248.2002.9715228.
[11] R. Manzel, W.O. Dörr, Manufacturing and irradiation experience with UO_2/Gd_2O_3 fuel, Am. Ceram. Soc. Bull. 59 (1980) 601–603.
[12] R. Yuda, K. Une, Effect of sintering atmosphere on the densification of UO_2-Gd_2O_3 compacts, J. Nucl. Mater. 178 (1991) 195–203.
[13] K.W. Song, K.S. Kim, J.H. Yang, K.W. Kang, Y.H. Jung, A mechanism for the sintered density decrease of UO_2-Gd_2O_3 pellets under an oxidizing atmosphere, J. Nucl. Mater. 288 (2001) 92–99. https://doi.org/10.1016/S0022-3115(00)00721-2.
[14] M. Durazzo, F.B.V. Oliveira, E.F. Urano de Carvalho, H.G. Riella, Phase studies in the UO_2–Gd_2O_3 system, J. Nucl. Mater. 400 (2010) 183–188. https://doi.org/10.1016/j.jnucmat.2010.03.001.
[15] M. Durazzo, A.M. Saliba-Silva, E.F. Urano de Carvalho, H.G. Riella, Sintering behavior of UO_2–Gd_2O_3 fuel: pore formation mechanism, J. Nucl. Mater. 433 (2013) 334–340. https://doi.org/10.1016/j.jnucmat.2012.09.033.
[16] H. Assmann, W. Dörr, Microstructure and density of UO_2 for light water reactors as related to powder properties, Mater. Sci. Monogr. 16 (1983) 707–718.
[17] M. Durazzo, H.G. Riella, Effect of mixed powder homogeneity on the UO_2-Gd_2O_3 nuclear fuel sintering behavior, Key Eng. Mater. 189–191 (2001) 60–66. 10.4028/www.scientific.net/KEM.189-191.60.
[18] D.R. Costa, F.J. Ezequiel, R. Gonzaga, S.H. Bernardelli, Individual influence of Al_2O_3 and Nb_2O_5 on grain growth of UO_2 sintered pellets manufactured at INB, in: International Nuclear Atlantic Conference. Associação Brasileira de Energia Nuclear-CNEN. Brazil, 2013.
[19] H. Assmann, M. Becker, Technology of UO_2 fuel fabrication by the AUC powder process, Trans. Am. Nucl. Soc. 31 (1979) 147–148.
[20] Inorganic Crystal Structure Database, Al, ICSD Collection Code 647594. FIZ Karlsruhe Leibniz Institute for Information Infrastructure. http://www2.fiz-karlsruhe.de/icsd_home.html?&cHash=0997f6804664b7e6fa8012358eef7f08.
[21] Inorganic Crystal Structure Database. Al, ICSD Collection Code 39185. FIZ Karlsruhe Leibniz Institute for Information Infrastructure. http://www2.fiz-karlsruhe.de/icsd_home.html?&cHash=0997f6804664b7e6fa8012358eef7f08.
[22] C.L. Yaws, The Yaws Handbook of Physical Properties for Hydrocarbons and Chemicals, Gulf Professional Publishing, Houston, Texas, 2015, p. 687.
[23] M.D. Larrañaga, R.J. Lewis, R.A. Lewis, Hawley's Condensed Chemical Dictionary, sixteenth ed., John Wiley & Sons, Inc., Hoboken, NJ, USA, 2016, p. 55, https://doi.org/10.1002/9781119312468.ch1.
[24] ASTM B962-08, Standard Test Methods for Density of Compacted or Sintered Powder Metallurgy (PM) Products Using Archimedes' Principle, ASTM International, West Conshohocken, PA, 2008.
[25] H. Assmann, M. Peehs, H. Roepenack, Survey of binary oxide fuel manufacturing and quality control, J. Nucl. Mater. 153 (1988) 115–126. https://doi.org/10.1016/0022-3115(88)90202-4.
[26] M. Peehs, W. Dörr, G. Gradel, G. Maier, Zur wärmeleitfähigkeit und plastizität von UO_2 mit Gd-zusätzen, J. Nucl. Mater. 106 (1982) 221–230 (in German), https://doi.org/10.1016/0022-3115(82)90351-8.
[27] International Atomic Energy Agency, Guidebook on Quality Control of Mixed Oxides and Gadolinium Bearing Fuels for Light Water Reactors, IAEA, Vienna, 1991, p. 59. IAEA-TECDOC-584.
[28] K. Une, Thermal expansion of UO_2–Gd_2O_3 fuel pellets, J. Nucl. Sci. Technol. 23 (1986) 1020–1022. https://doi.org/10.1080/18811248.1986.9735090.
[29] S. Fukushima, T. Ohmichi, A. Maeda, H. Watanabe, The effect of gadolinium content on the thermal conductivity of near-stoichiometric $(U,Gd)O_2$ solid solutions, J. Nucl. Mater. 105 (1982) 201–210. https://doi.org/10.1016/0022-3115(82)90375-0.
[30] A.V. Fedotov, E.N. Mikheev, A.V. Lysikov, V.V. Novikov, Theoretical and experimental density of $(U,Gd)O_2$ and $(U,Er)O_2$, Atom. Energy 113 (2013) 429–434. https://doi.org/10.1007/s10512-013-9657-3.
[31] H.G. Riella, M. Durazzo, M. Hirata, R.A. Nogueira, UO_2-Gd_2O_3 solid solution formation from wet and dry processes, J. Nucl. Mater. 178 (1991) 204–211. https://doi.org/10.1016/0022-3115(91)90387-M.
[32] S.-H. Kim, Y.-G. Kim, H.-S. Kim, S.-H. Na, Y.-W. Lee, D.-S. Suhr, Thermal conductivity of near-stoichiometric $(U,Er)O_2$ solid solutions, J. Nucl. Mater. 342 (2005) 119–124. https://doi.org/10.1016/j.jnucmat.2005.03.020.
[33] S. Yamanaka, K. Kurosaki, M. Katayama, J. Adachi, M. Uno, T. Kuroishi, M. Yamasaki, Thermal and mechanical properties of $(U,Er)O_2$, J. Nucl. Mater. 389 (2009) 115–118. https://doi.org/10.1016/j.jnucmat.2009.01.016.
[34] S.M. Ho, K.C. Radford, Structural chemistry of solid solutions in the UO_2-Gd_2O_3 system, Nucl. Technol. 73 (1986) 350–360. https://doi.org/10.13182/NT86-A16077.
[35] M. Durazzo, A.M. Saliba-Silva, E.F. Urano de Carvalho, H.G. Riella, Remarks on the sintering behavior of UO_2–Gd_2O_3 fuel, J. Nucl. Mater. 405 (2010) 203–205. https://doi.org/10.1016/j.jnucmat.2010.08.002.